CIMAC CONGRESS 25
ZURICH, MAY 19 – 23, 2025

2025 | 060

Optical visualization of performance-limiting combustion phenomena in marine and stationary hydrogen engines

Visualizations

Sven Ole Deist, TU Munich, Institute of Sustainable Mobile Powertrains

Wilhelm Dürrholder, TU Munich, Institute of Sustainable Mobile Powertrains
Dominik Winkler, MAN Energy Solutions ES
Kay Mahler, WTZ Roßlau
Maximilian Prager, TU Munich, Institute of Sustainable Mobile Powertrains
Malte Jaensch, TU Munich, Institute of Sustainable Mobile Powertrains

ABSTRACT

Hydrogen as an energy carrier represents a future-oriented option for the decarbonization of combustion processes in large-bore engines. Hydrogen-based chemical compounds like ammonia and methanol, as well as pure hydrogen itself, offer a carbon-free alternative for marine and stationary applications. For economical implementations, retrofit solutions in mono- and dual-fuel engines are of interest. For the use of 100% hydrogen, the limiting combustion phenomena such as pre-ignition and backfire - favored due to the medium's fast flame propagation, low quenching distance, and low ignition energy - must be handled appropriately. A precise consideration of these statistically occurring combustion anomalies and their temporal-spatial relationships, which cannot be resolved through thermodynamic measurements alone, is essential and requires further understanding. For this reason, and within the scope of this article, a conventional medium-speed single-cylinder engine with a bore diameter of 350mm and a displacement volume of 42.3 l is optically investigated with 100% hydrogen, and power densities up to more than 20 bar indicated mean effective pressure. Using varying air-fuel ratios between 2.3 and 4.0 and imaginary data, engine operation limits caused by combustion anomalies are identified while comparing a pre-chamber and an open chamber ignition system. Via two endoscopic access, images are recorded using up to three high-speed cameras simultaneously to capture the luminescence in the visible and the ultra-violet spectrum at around 308 nm to make the chemiluminescence signal of hydroxyl radicals visible. Abnormal combustion events trigger the camera system and capture the images in a ring buffer. The temporally classified pre-ignitions reveal the flame propagation after ignition. In this process, backfire events resulting from pre-ignition dominate and define the load limit of the engine. The origins of these combustion anomalies can increasingly be localized to the area around one of the intake valves. As the load increases, this region dissipates, leading to distributed combustion initiations and piston side ignitions. This behavior is likely explained by the load-dependent increase in surface temperature in combination with the geometry of the intake manifold and the density differences of hydrogen and air, which contribute to the dehomogenization of the mixture. The presented findings serve as a foundation for future experimental and simulation-based investigations.

1 INTRODUCTION

Combustion processes in large-bore combustion engines remain essential for long-haul, robust, and continuously operating stationary or maritime applications. Electrification has not yet provided the required power densities and peak loads over extended periods. [1–3] To economically minimize or even eliminate carbon emissions in combustion systems, retrofit solutions and multi-fuel concepts for existing combustion engines utilizing alternative fuels, such as hydrogen, are being investigated and partially implemented [4; 5]. To accelerate this progress and additionally address the challenges posed by climate change and rising energy consumption in the overall transport sector, over 40 countries worldwide have committed by 2024 to establishing hydrogen as a key energy carrier, formulating hydrogen strategies, and allocating subsidies [6; 7].

Hydrogen, in chemical derivatives such as ammonia or methanol or in its pure form, represents a viable substitute for diesel, heavy fuel oil, and natural gas [3; 8]. However, when considering pure hydrogen, several challenges arise, including its energy-intensive production, storage, and transport, primarily due to its low volumetric energy density. Moreover, its application as a combustion fuel poses significant technical difficulties, as hydrogen exhibits higher burning velocities, lower ignition energy requirements, wider ignition limits, reduced quenching distances, and greater diffusion behavior compared to fossil fuels such as diesel and natural gas [3; 9; 10]. A comparison of the mentioned fuels is shown in Table 1.

Table 1. Comparison of fuel properties (p=1.013 bar, T=25°C) [3; 11; 12]

	H_2	CH_4	Diesel
Molar Mass [kg/kmol]	2.02	16.04	190
Density [kg/m^3]	0.09	0.717	840
Laminar Flame speed[1] [cm/s]	2.30	0.42	0.4
Quenching Distance[1] [mm]	0.64	2.5	-
Diffusion Coefficient [cm^2/s]	0.61	0.16	-
Ignition Energy[1] [mJ]	0.017	0.29	0.24
Ignition Limits [vol.-%]	4-75	4.4-15	0.6-5.5

[1] For Air Fuel Ratio = 1

These properties favor stochastically occurring combustion phenomena, called combustion anomalies, which currently represent the primary performance-limiting factor for hydrogen-powered engines [13; 14]. Combustion anomalies originate from temporal and spatial abnormal ignition events. These anomalies are categorized based on the timing of the abnormal ignition, while the location provides insight into their causes. Pre-ignitions occur before the intended ignition timing, resulting in backfire, and/or excessive pressure rises within the combustion chamber. Their causes include hot spots, such as heated lubricating oil, thermally stressed component surfaces, hot gas, or particulate deposits from previous operating cycles. Ignition events near or after the intended ignition point often manifest as engine-knocking behavior.

To extend the operational limits of large hydrogen engines to full-load conditions, the spatiotemporal dependency of combustion anomalies must be resolved. This cannot be achieved through purely thermodynamic analyses, necessitating optically accessible engines. Such investigations can be performed maximally invasive using side windows and glass pistons in the Bowditch structure [15] or minimally invasive through endoscopic access [16; 17].

When employing optically accessible engines, it must be considered that the increase in clearance volumes and differences in the thermal properties of components lead to variations in combustion durations, efficiencies, and engine stability. This was demonstrated by Karmann [18] in a comparative study of optical and full-metal engine designs and needs to be respected.

To achieve realistic operation, engine modifications are minimized. In this study, endoscopic access points are integrated into the engine to investigate the origins of abnormal combustion phenomena in a conventional medium-speed, large hydrogen engine with a 350 mm bore and a 440 mm stroke corresponding to a 42.3 L displacement volume. These investigations are conducted under varying parameters using optical imaging in the visible and ultraviolet (UV) spectra.

2 STATE OF RESEARCH

Recent research aimed at improving the performance of hydrogen engines, mainly focusing on combustion anomalies, underscores the growing interest and urgency surrounding this technology. However, investigations on large bore engines are limited.

Eicheldinger et al. [19] conducted maximum load tests using 100% hydrogen in a 4.8 L single-cylinder high-speed hydrogen engine. The operational limits were defined based on the occurrence of combustion anomalies. A compression ratio of 9.6 and the addition of water injection up to 34 kg/h indicated mean effective pressures (IMEP) exceeding 40 bar were achieved. The study demonstrated that, in terms of load enhancement, water injection effectively complements the compression ratio reduction. The

cooling effect of water injection also led to decreased nitrogen oxide (NO_x) emissions.

Eicheldinger and Karmann [13] performed thermodynamic and optical investigations of backfire phenomena on the same 4.8 L high-speed engine. The results indicated that abnormal ignitions were caused by residual gas at the exhaust valve, with exhaust backpressure having the most significant influence on backfire behavior. Furthermore, no blackbody thermal radiation was observed, indicating the absence of lubricant oil ignition (LOI).

However, the interaction between lubricating oil and hydrogen remains critical, as suggested by Distaso et al. [20–22]. Numerical investigations explored the interactions between hydrogen and lubricating oil and the mechanisms underlying LOI. It was shown that the process of LOI can commence below the ignition temperature of hydrogen, as lubricating oil exhibits increased reactivity, manifesting as a "cool flame" even at relatively low temperatures.

The relevance of the oil-hydrogen interaction and the resulting lubricating oil ignition was also investigated by Gschiel et al. [23] to compare different oils in engines with varying sizes, up to a bore of 139 mm and a stroke of 161 mm, a dosing method was developed to experimentally assess the influence of the oil on early ignition behavior.

Additional optical investigations revealed that combustion anomalies are characterized by increased light emissions due to faster combustion and higher heat release rates, particularly in the presence of LOI [24–26]. Feng et al. [26] further described that the heat release from deflagration propagation, initiated by a pre-ignition event, compresses the unburned gas. This compression increases pressure and temperature in the unburned gas, potentially igniting it or causing pressure inhomogeneities that manifest as pressure oscillations. These oscillations, in turn, can release lubricating oil from the piston ring pack, leading to subsequent anomalous events.

Yang et al. [27] identified additional factors influencing combustion anomalies in hydrogen operation through experiments on a single-cylinder port fuel injection (PFI) hydrogen engine with a bore and stroke of 94 mm and 85 mm, respectively. They examined the influence on backfire events by varying the injection quantity and geometric injection angle in the intake manifold. Injection angles smaller than 45°, relative to the intake manifold axis, resulted in more inhomogeneous mixtures within the combustion chamber. During the compression phase, rich mixtures near the intake valve increased the likelihood of backfire.

In general, mixture formation within the intake system and the combustion chamber has primarily been addressed in numerical studies in various publications [19; 28–30].

Rajavsanth et al. [31] investigated a targeted hot-spot-induced pre-ignition in a 2.34 L direct injection (DI) hydrogen engine. A temperature-controlled glow plug within the combustion chamber served as the ignition source for abnormal events. Initial ignitions were only achieved at temperatures exceeding 1100K at the glow plug, concluding that surface ignitions on engine components are unlikely, as such temperatures are typically not reached by components. Additionally, it was observed that boosted inlet pressures reduce the probability of pre-ignition. This is established by sharply increased ignition delay times at elevated pressures through, for example, turbocharging.

Turbocharging as a means to extend operating limits was also employed by Wittek et al. [32] when retrofitting a 3.6 L diesel engine to operate as a PFI hydrogen engine, particularly in lean-burn conditions, charged air is required to achieve a high torque outcome.

Exhaust gas recirculation (EGR) represents another method to enhance load limits. Similar to water injection, EGR reduces combustion chamber temperatures. Lowering peak temperatures decreases NO_x emissions and improves efficiency [33]. The reduced reactivity of the mixture lowers the probability of anomalies occurring in the combustion chamber and the intake duct. Lu et al. [34] demonstrated a backfire map as a function of engine speed (1000–1800 rpm), air-fuel ratio (AFR), and start of injection (SOI). Larger backfire zones were observed at lower engine speeds (~1000 rpm), but these zones were significantly reduced by employing 12% EGR. Shinde et al. [35] further noted that dehumidified EGR enhances performance.

All the improvements over the last decades resulted in the first successful implementation of a hydrogen-capable two-stroke engine in early 2024 by the Japanese company Mitsui E&S Co., utilizing a MAN B&M 4S50ME-T engine. This engine demonstrated variable power densities up to 100% load with 100% hydrogen as the fuel source. [36]

The operation of medium-speed, large hydrogen engines with optical accessibility, particularly in the context of combustion anomalies, is the aim of this study but has not been reported in the literature.

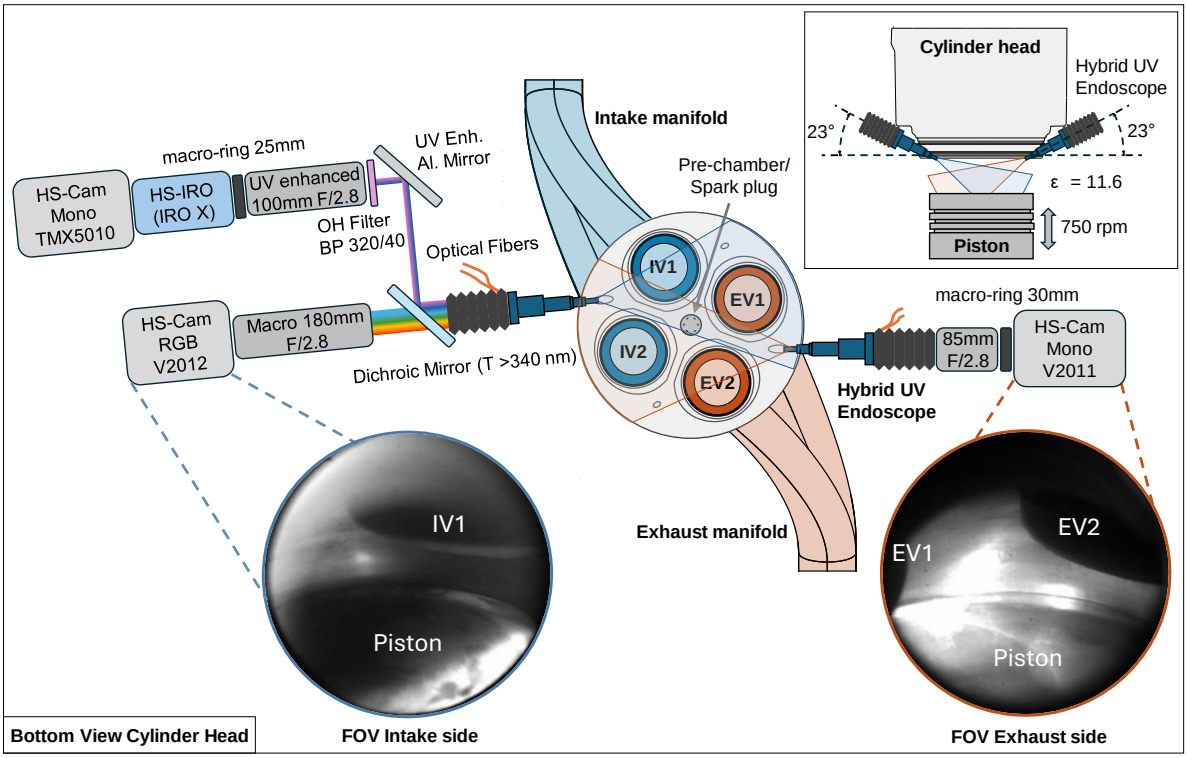

Figure 1: Schematic structure of the optical test bench periphery. View of the cylinder head from below and from the side.

3 EXPERIMENTAL SETUP

As part of the research project “Hydrogen Powered Large Engines” (HydroPoLEn), a minimally invasive optical examination of a single-cylinder research engine is conducted in this study. The conventional medium-speed, four-stroke engine, equipped with a PFI system, operated with a Miller valve timing and a valve overlap, features two optical access points that pass through the water jacket and cylinder head into the combustion chamber at an angle of 23°. The first access is between the intake valves (IV1 and IV2) on the intake side, and the second access is on the exhaust side between the exhaust valves (EV1 and EV2). Figure 1 illustrates the optical test bench and its periphery. Optical access is enabled using a hybrid UV high-efficiency endoscope (F2.8) from Lavision, which has been modified to ensure functionality, tightness, and cooling. The critical temperature limit of the endoscope's front lens, set at 200°C, is maintained using a double-walled sleeve with air cooling [16; 19]. Measurements taken in this study with an integrated thermocouple positioned behind the sapphire protective glass indicated a cooling effect of 40°C. The endoscope offers a field angle of roughly 50°.

The optical path extends from the endoscope to the camera system, which is mechanically decoupled from the endoscope and the engine. Vibrations of up to 15 mm in the horizontal direction, caused by the testbed's pneumatic air suspension, result in relative movements between the engine and the camera, leading to a shifting field of view (FOV) on the camera sensor. Two optical fibers for each endoscope were embedded within the endoscope and aligned with the camera to counteract these vibrations optically. These fibers capture reference light points that compensate for the recorded vibrations.

The imaging system comprises three high-speed cameras that observe the combustion chamber via two optical access points. Through the access between the two IVs, the combustion chamber is captured in the visible spectrum using a Phantom v2012 RGB camera equipped with a macro lens (f = 180 mm; F2.8). A dichroic mirror (reflection < 340 nm < transmission) enables simultaneous detection of hydroxyl radical (OH radical) emissions at around 308 nm using a Phantom TMX 5010 monochrome camera with a high-speed image intensifier (S20 photocathode, P46 phosphor screen, gate: 80 ms, gain: 65%), a UV-optimized lens (f = 100 mm; F2.8), and an optical bandpass filter (300–340 nm, transmission above 70 %). Images between the exhaust valves are captured by a Phantom v2011 monochrome camera paired with a UV-optimized lens (f = 85 mm; F8). The FOV size is fine-tuned using macro rings between the camera and lens. The respective FOV partially captures the movement of the piston

and the intake and exhaust valves. The piston edge can be seen in the range of CA ≈ 25° - 100° before and after the top dead center (TDC). Figure 1 contains a representative view of the two perspectives. The depth of field is shallower due to the different structures on the intake side. Additionally, the installation position of the endoscopes imposes a limitation on the FOV. This is evident as a crescent-shaped artifact at the upper edge of the FOV, representing the occluded portion of the combustion chamber roof.

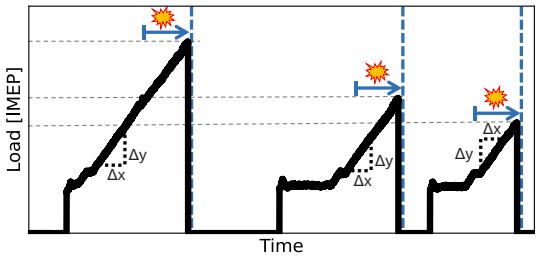

Figure 2: Load ramps with constant slope until the abnormal event.

Figure 2 depicts the test procedure. Load ramps are conducted until abnormal combustion occurs under constant AFR, a constant engine speed of 750 rpm, and synthetic oil as the lubricant. These events triggered the camera system, which retroactively stored 8,000 images using a ring buffer. The cameras operated at a frequency of 9 kHz, corresponding to a crank angle (CA) resolution of approximately 0.5° at the specified speed.

Table 2. Engine Properties and boundary conditions.

Displacement	42.3 L
Bore	350 mm
Stroke	440 mm
Number of Valves	4
Compression ratio	11.8:1
Engine speed	750 rpm
Inlet Air Temperature	50 °C
Oil Temperature	65 °C
Cooling Water Temperature	90 °C

For standardization, the engine was calibrated using an initial measurement under constant media temperature conditions. During operation, a stable performance was achieved with a coefficient of variation (COV) of less than 2%.

Subsequent tests included variations in AFR (λ = 2.3–4.0) and ignition concepts, utilizing both open combustion chambers and active pre-chamber ignition systems. The ignition systems are located in the cylinder head center. An overview of the engine data and boundary conditions are listed in Table 2.

4 IMAGE POST-PROCESSING

The images captured by the three cameras undergo post-processing steps to filter and analyze events within the FOV. Figure 3 illustrates the processing procedure for simultaneous recording of the visible and UV spectra.

As described above, a ring buffer is employed to

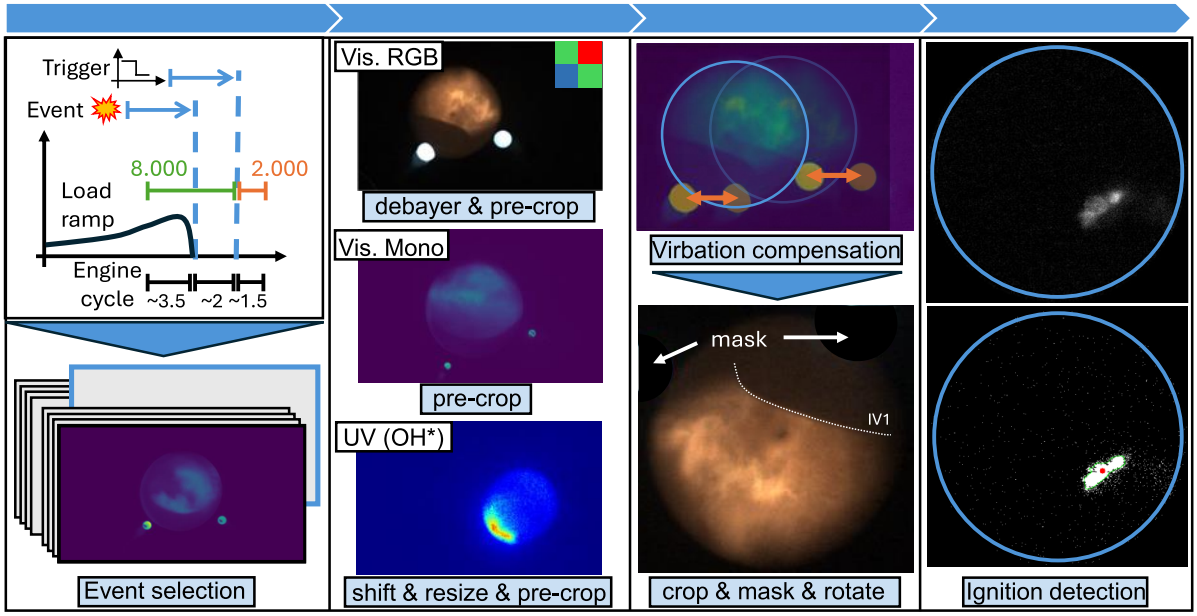

Figure 3: Post-processing procedure. Event selection and data reduction followed by background subtraction, vibration compensation, FOV cropping, and intensity-based flame detection.

record stochastic events. This approach enables the capture of anomalies along with the three preceding engine cycles. The CA is determined based on the recording frequency, engine speed, and event trigger. TDC is at CA=0°. Automatic assignment is not feasible when utilizing the ring buffer. After the manual assignment, specific CA ranges can be filtered from the image data. Deviations in the pressure signal identify the anomalies during the event. Subsequently, the reduced data undergo a debayer, pre-cropping, and background subtraction procedure. Optical vibration compensation is then performed using two reference light points. The wavelength of these reference light points exceeds the reflection limit of the dichroic mirror, ensuring that the image intensifier remains unaffected by local overexposure. Vibration compensation for the UV range is achieved via the visible optical path, with adjustments made to the size and position of the respective FOV.

It is important to note that the light points do not lie within the intermediate image plane of the endoscope, resulting in a perspective error and relative motion between the light points and the FOV. The perspective offset is recalibrated for each measurement day and accounted for during vibration compensation.

The compensated images are cropped to the FOV and overlaid with a mask for the reference light points, which slightly intrude into the FOV on the inlet side.

After binarization of the images, intensity-based object detection is applied to identify the origins of combustion. The combustion origin, or its initial detection, is determined based on the object's area, orientation, eccentricity, and center.

The piston and valve contours are interpolated from combustion chamber images and the corresponding stroke.

5 RESULTS AND DISCUSSION

The series of measurements examined the influence of AFR variations and different ignition concepts on combustion behavior. The load ramps resulted in IMEP of ±7 bar with stable combustion around the medium load range. The observed combustion anomalies were limited to events occurring before the actual ignition point and were categorized into backfire and early and late pre-ignition.

"Regular" combustions (RC) are plotted as a reference for anomalous operating cycles. A representative pre-chamber-ignited combustion is depicted in Figure 4. Thereby, the light intensity in the monochromatic images is normalized to its respective maximum. The sensors' maximum achievable intensity scales the RGB image. In both recorded perspectives, one or two pre-chamber flares are visible shortly after the ignition point, following the pressure peak in the pre-chamber. These flares propagate from the top left into the field of view. Despite combusting a pure hydrogen-air mixture, partially visible light emissions were observed in the wavelength range of 500–600 nm in an orange color. This phenomenon is attributed to oil vapor in the pre-chamber during the compression phase, which manifests as thermal blackbody radiation during combustion. Notably, the intensity of the orange light emission varies but increases with rising load and decreases for leaner AFR conditions.

Following ignition by the pre-chamber flares, the hydrogen-air mixture in the main combustion chamber ignites, rapidly increasing light intensity corresponding to the heat release rate. This often causes transient overexposure of the cameras configured to capture the combustion anomalies. The light emissions subside at approximately 20° CA after the center of combustion.

The downward piston movement becomes visible from around 30° CA after TDC. Of particular note are the glowing areas observed at various points during the expansion phase at the piston edge. These glowing areas correspond to oil residues, which undergo residual reactions and emit visible radiation. However, the localized elevation in temperature does not create further ignition sources, as the hydrogen-air mixture has already burned out due to its high burning rate.

Oil droplets are wiped off from the piston edge onto the liner wall during the entire downward movement of the piston, up to approximately 100° CA after TDC. However, a direct spatial correlation between the glowing oil droplets observed in the FOV in prior working cycles and the abnormal combustion event cannot be established. It is, therefore, hypothesized that pre-reacted oil remains on the liner wall and is ejected into the combustion chamber during the subsequent compression phase due to rising pressure or piston motion, increasing the likelihood of LOI.

This behavior could not be observed in experiments utilizing an open combustion chamber equipped with a centrally located surface discharge spark plug in the cylinder head, as opposed to a pre-chamber configuration. It should be noted that the loads achieved for an AFR in the range of 2.5

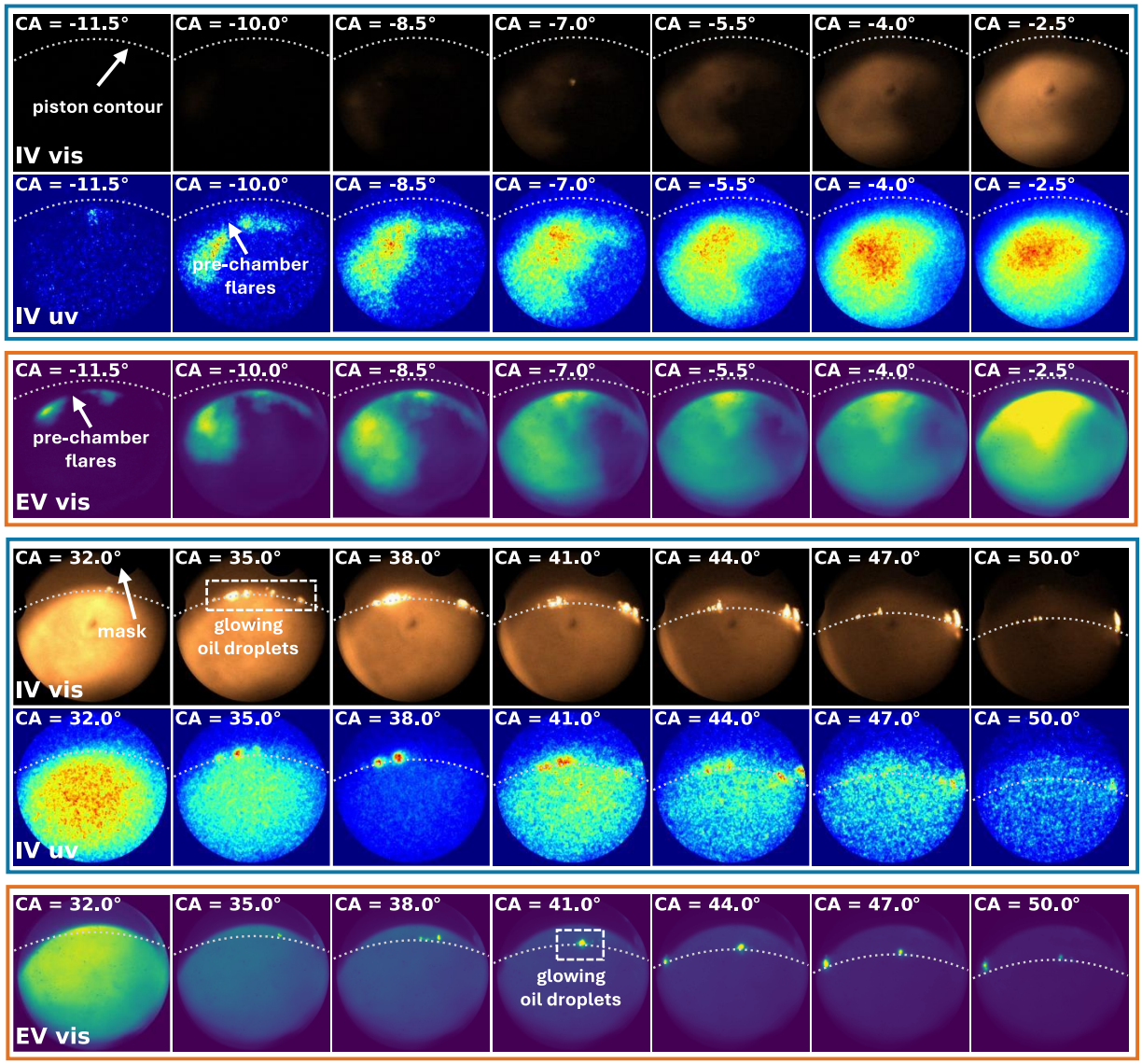

Figure 4: Regular combustion in pre-chamber setup. Pre-chamber flare development and glowing oil droplets during expansion phase. . λ = 2.5, 16 bar IMEP

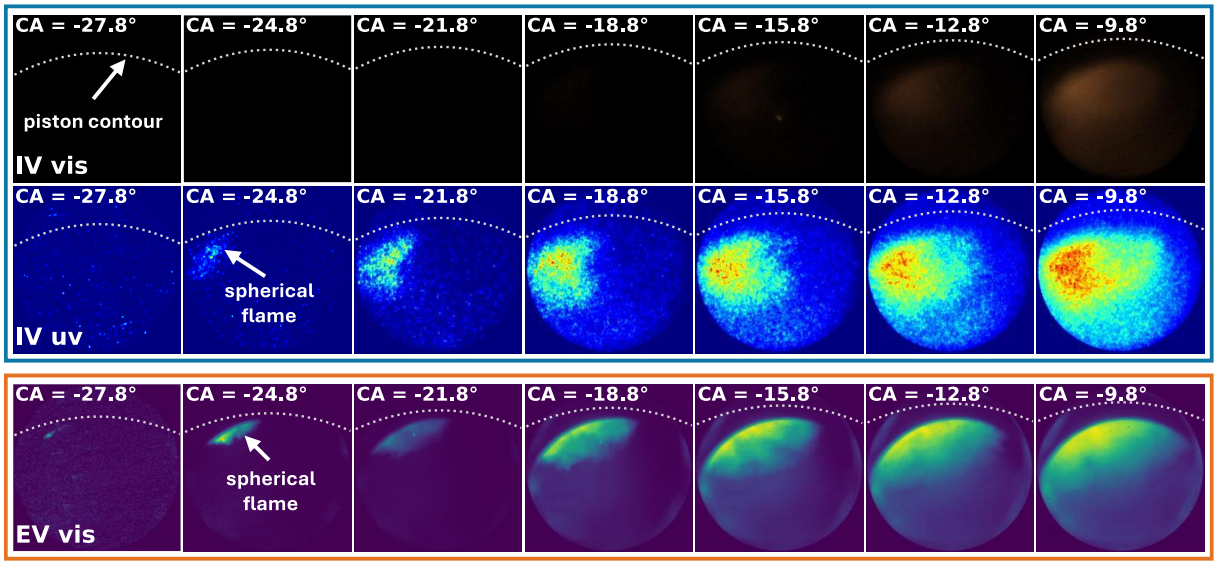

Figure 5: Regular combustion in open chamber setup. Spherical flame development from spark plug ignition. λ = 2.5, 13 bar IMEP.

are 20 – 40 % lower than those achieved with the pre-chamber configuration. No glowing particles are observed in either configuration for lean mixtures with λ = 4.0 and comparable loads. Figure 5 depicts a regular combustion event within an open combustion chamber characterized by a spherical flame propagation pattern. As in previous observations, flame propagation is visible due to increased light intensity and the combustion of oil residues, a consequence of heat release. Direct interaction between the flame and the combustion chamber roof, along with possible oil mist or residues at the onset of combustion, results in blackbody radiation.

phenomena, as the flame propagates into the intake manifold while the IVs remain open. Late early ignition, by contrast, results in premature pressure increases during compression. Figures 6-9 illustrate four distinct pressure traces and their corresponding optical recordings. In the following RGB images, the intensity is also normalized with the respective maximum due to lower emission at lower pressure.

Figure 6 shows a backfire event initiated by early ignition at -292.3° CA. Under these conditions, the intake valves are fully open, and the pressure signal rises before decaying as pressure escapes

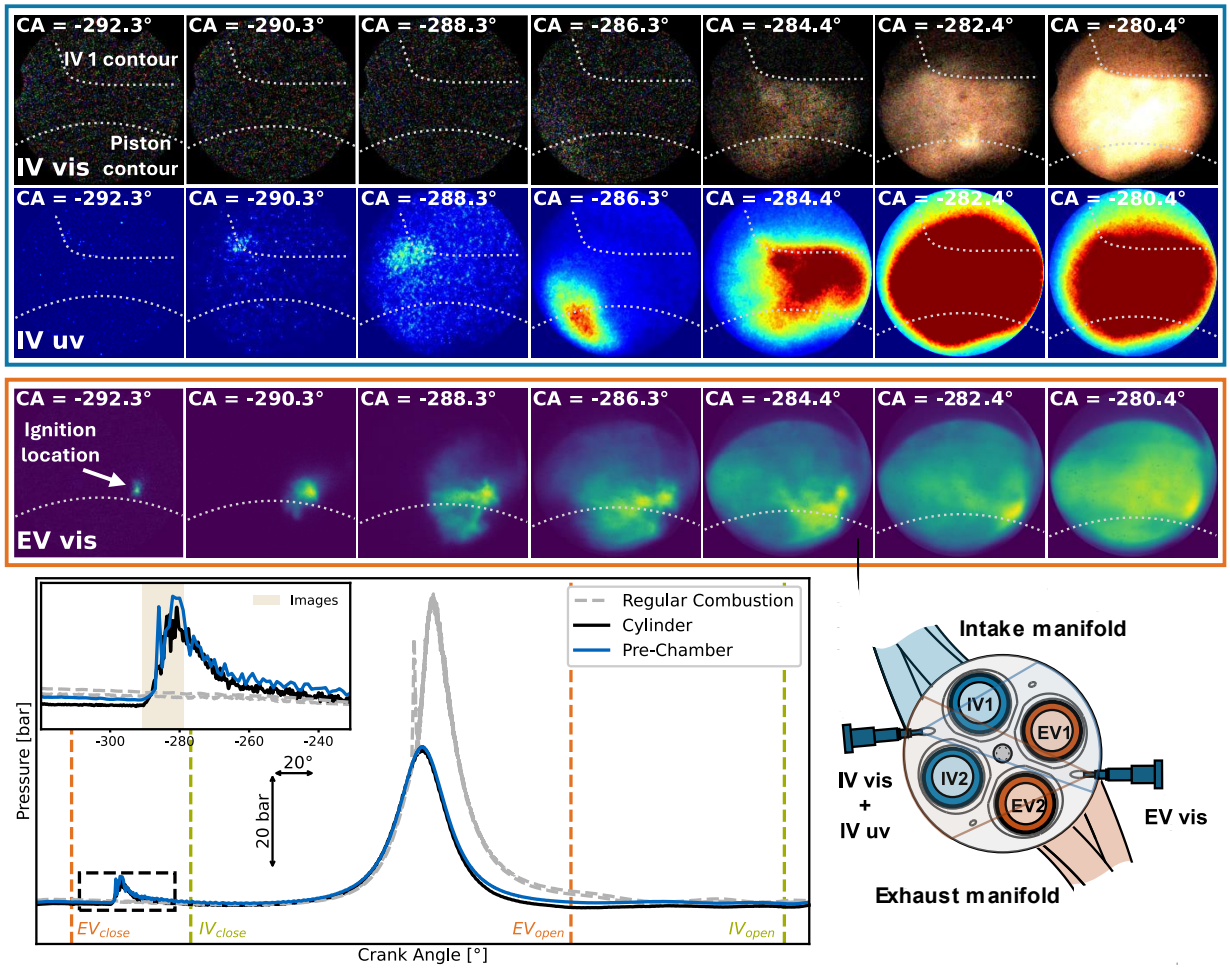

Figure 6: Backfire during full open Intake valves. Two perspectives visualizing the visible and OH radical emissions. Initial Ignition close to the piston edge below the intake valves. λ = 2.5, 15 bar IMEP.

In contrast to the pre-chamber flares, which transport the flame and associated thermal energy faster and preferentially toward the piston edge region, no glowing oil droplets are observed under the conditions of spherical flame propagation.

The regular combustion cycles are juxtaposed with the recorded anomalous combustion events. These anomalies primarily manifest as early ignition events occurring at various CAs. Early ignition during the intake phase leads to backfire into the intake manifold. In this case, λ = 2.5 and 15 bar IMEP, ignition occurs within the FOV near the piston edge on the exhaust side below the IVs. The position of ignition suggests, with respect to the visible light emissions and the glowing oil droplets during regular combustion, an indication of a LOI.

If premature ignition occurs while the IVs are closing, backfire can result. However, the pressure buildup cannot dissipate until the valves are fully

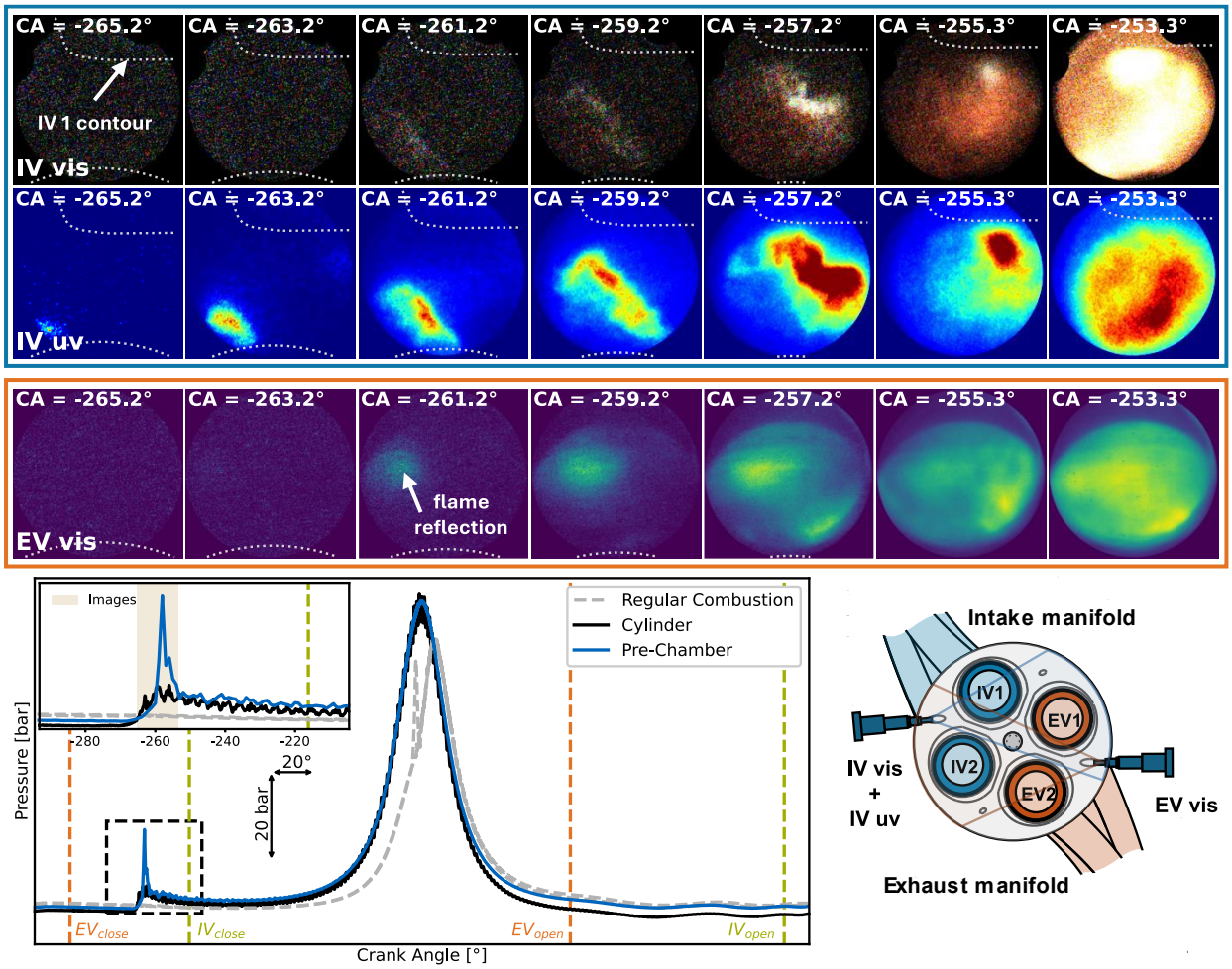

Figure 7: Backfire during closing Intake valves. Two perspectives visualizing the visible and OH radical emissions. Initial ignition evolves close to piston edge and propagates to the IV. .λ = 2.7, 15.4 bar IMEP.

closed. This scenario is illustrated in Figure 7, where initial ignition occurs at -265.2°. The flame front originates on the piston side beneath the EVs and propagates through the combustion chamber toward the IVs. As the flame front encounters increasing amounts of fuel, the heat release and light emissions intensify.

The RGB images depict the combustion of hydrogen in a bright white color, representing the rapid combustion occurring along the flame front. In contrast, the orange blackbody radiation, likely originating from oil residues in the piston edge area, follows the hydrogen flame. Additionally, reflections of the flame on the liner are visible on the exhaust side before the main flame front becomes apparent.

An additional rise in pre-chamber pressure is evident in the corresponding pressure trace and intensifies the light emissions in the optical recordings. This discrepancy suggests the ignition of gas previously accumulated in the pre-chamber. A similar pre-chamber pressure peak is visible in Figure 8 during a late backfire event.

In Figure 8, ignition of the hydrogen-air mixture occurs at -245.8° CA. Here, the IVs are almost closed, limiting pressure relief after the initial pressure rise in the main combustion chamber, even though the flame directly starts propagating to the IVs. The chamber pressure rises prematurely and overshoots the maximum peak pressure of the regular combustion. Visible light emissions are first noted after the pre-chamber peak causing weak flares propagating into the FOV. The events in Figure 8 exhibit UV light emissions extending up to the actual ignition point. Ignition during the expansion phase is substantially delayed due to the slightly negative pressure induced by the Miller cycle. This behavior can be attributed to charge motion and the resulting temporary stabilization of the flame.

After the backfire, the pressure oscillations in the main combustion chamber are caused by the propagating pressure waves from the combustion detonations. The geometry of the combustion chamber determines the frequency. With closed IVs, these oscillations persist until the pressure maximum, as shown in Figures 7 and 8.

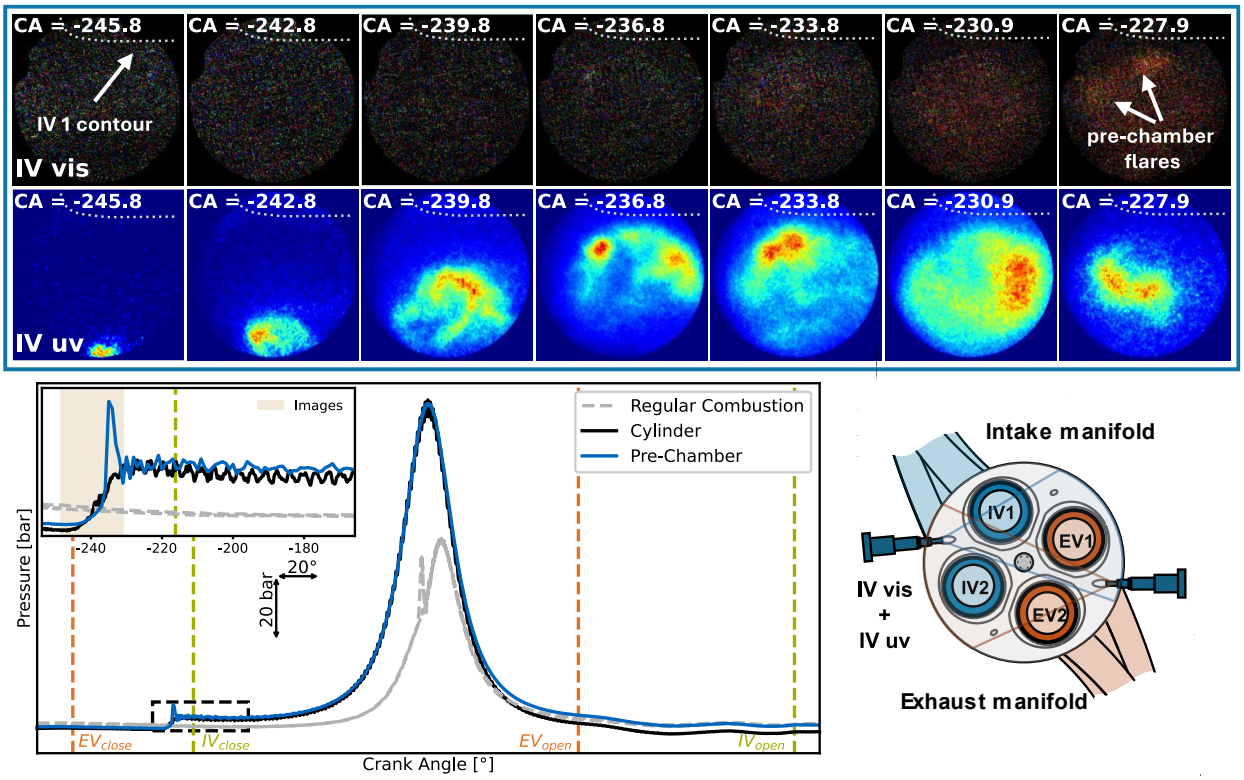

Figure 8: Late backfire while Intake valves are almost closed. Flame development in the OH radical emissions spectrum. Initial Ignition evolves close to piston edge. Small pre-chamber flares due to pressure peak. λ = 3.0, 14.7 bar IMEP.

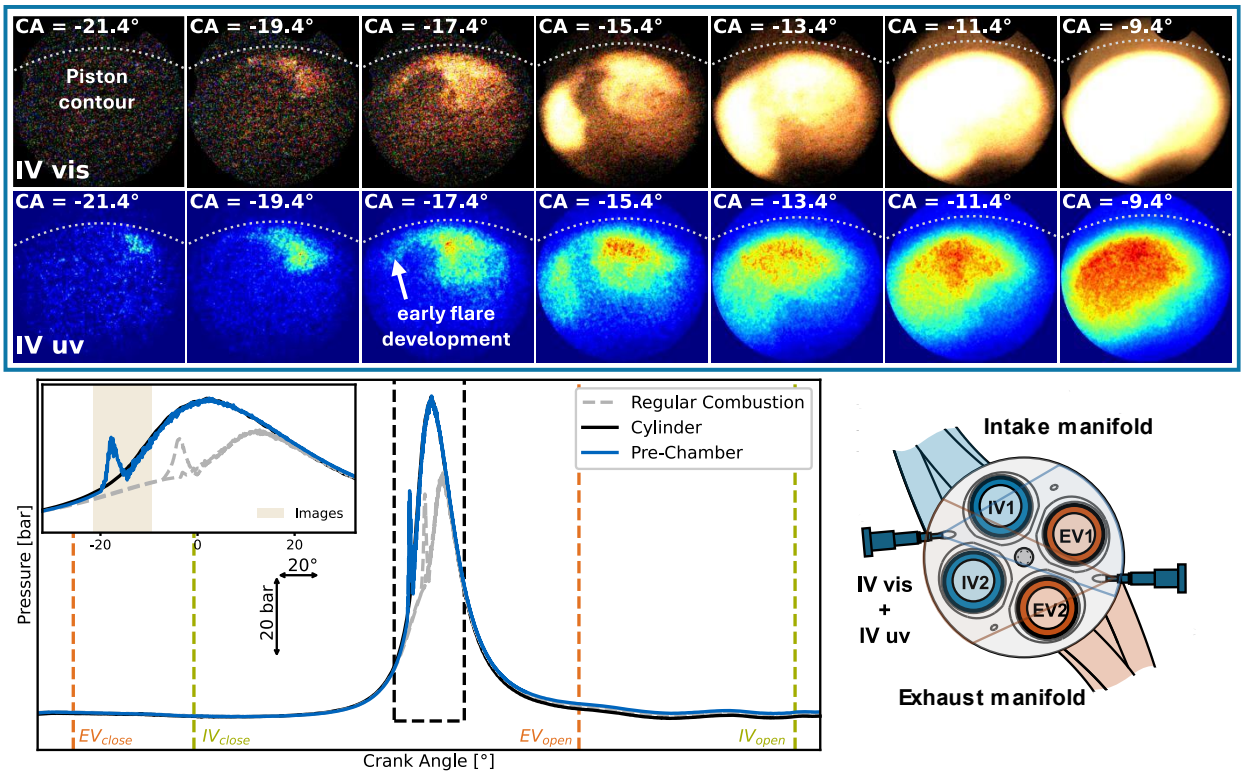

Figure 9: Pre-ignition event causing pressure overshoot. Flame development in the visible and OH radical emission spectrum from the intake side. Initial ignition evolves from chamber roof. λ = 2.5, 14 bar IMEP.

Figure 9 demonstrates a late early ignition event at -21.4° CA, where compression is underway. Consequently, a rapid pressure rise occurs, surpassing the pressure levels associated with regular combustion at an early stage.

A comparative analysis of the pressure curves from the main combustion chamber and pre-chamber confirms that no pre-chamber pre-ignition was detected. Therefore, hot residual gases in the pre-chamber can be excluded as a cause of pre-ignition. However, pre-ignition originating near the pre-chamber cap within the combustion chamber cannot be entirely ruled out.

gray markers indicate flame detections recorded by cameras that did not capture the combustion event first.

The distribution of the initial ignition positions in Figure 10 reveals a concentration of numerous detections in the area to the right of the FOV on the intake side. This can be attributed to flame propagations originating from the right. From the perspective of the exhaust side, this manifests as an accumulation of detections on the left side (gray). The region of increased initial ignition occurrence corresponds to the position between IV1 and EV1. Since, as depicted in Figure 1, the

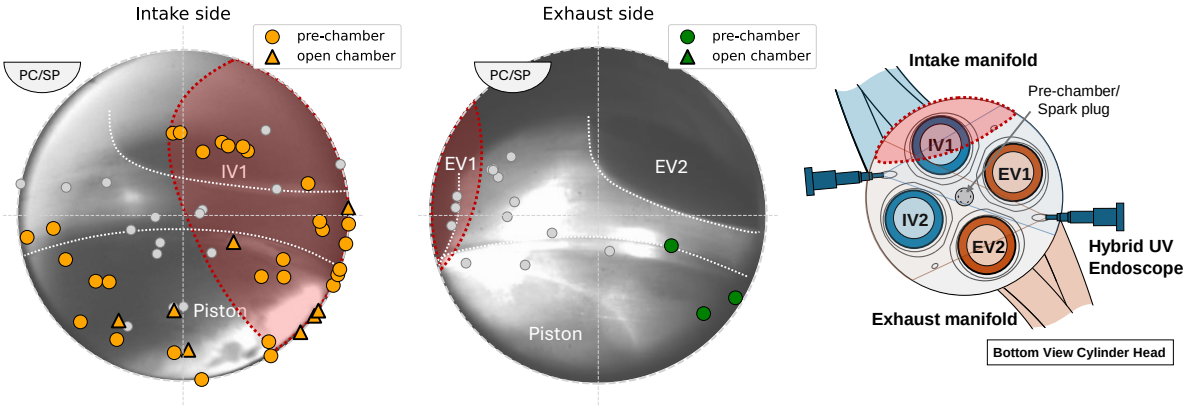

Figure 10: Initial Ignition position distribution of backfire events with pre-chamber (circle) and open chamber (triangle) ignition system. The colored scatter points indicate the first ignition detection, the gray scatter points indicate the subsequent detection of the other cameras. λ = 2.3 – 4.0.

All measurements were subjected to object detection analysis to determine the origin of abnormal combustion, as illustrated in Figure 3. The combustion origins within the respective FOV are mapped in Figure 10. Background images are used for spatial orientation within the FOV but do not correspond to the precise ignition timing of each event.

Color-coded detection results indicate that most abnormal combustion events near the inlet side, observed in the UV spectrum, are attributed to OH radical emissions (orange). While sooty combustion caused by oil cannot be excluded entirely, these findings strongly suggest that residual gas or hot-spot ignition is as dominant as LOI. The RGB camera, which has limited sensitivity to light emissions, primarily detects faint emission silhouettes, typically white-bluish or slightly orange in color. An initial ignition could not be assigned to the RGB camera. The monochrome camera (green), with a spectral sensitivity extending into the long-wave UV range (10% quantum efficiency at 370 nm), provides a comprehensive view of the combustion propagation process within the FOV, closely resembling the OH radical emissions. The

FOV also includes the area beneath EV1, the origin can reasonably be assumed to be in the direction of IV1. This hypothesis is supported by the observation that some flame fronts show no propagation into the FOV. Still, the detected object appears in the FOV within 0.5° CA, corresponding to 110 µs at 750 rpm. Therefore, an initial ignition near the endoscope access, viewed in the direction of the image plane, is probable. In addition, the first detections in the valve stroke area of IV1 occur while the IVs are open, indicating flame propagation from a spatial perspective in front of IV1.

The red region's accumulation indicates a potentially richer region near the IV1, resulting from density stratification. As shown in Figure 1, the test engine does not possess a symmetric intake flow for both IVs; instead, the flow enters from the side. Consequently, the distance to IV1 is longer than to IV2. The fuel-air mixture, consisting of hydrogen with a density of 0.09 kg/m^3 and air with a 1.225 kg/m^3 density under standard conditions, is subjected to different inertial forces depending on the component. The higher density and resultant mass inertia of air lead to a more stable flow, which

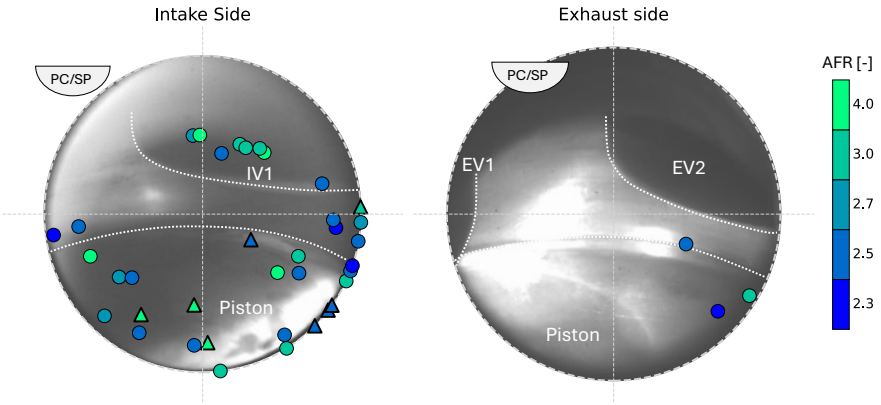

Figure 11: AFR dependent initial ignition position distribution of backfire events with pre-chamber (circle) and open chamber (triangle) ignition system.

displaces the hydrogen and pushes it ahead. In addition, the outside curvature of the intake manifolds of IV2 also ensures a centrifugal air movement towards IV2. This process might result in dehomogenization over the length of the intake path. The longer outer path to IV2 leads to a leaner mixture than the global AFR. Conversely, the mixture near IV1 experiences enrichment in the intake manifold, leading to local enrichment within the combustion chamber. As reflected in the recorded data, this localized enrichment enables earlier attainment of the necessary ignition conditions, increasing the risk of pre-ignition.

An AFR dependency of the accumulation and the initial ignition position in general could not be identified, as depicted in Figure 11. In addition to the spatial analysis, the temporal evaluation also revealed no dependence on the AFR.

When analyzing the influence of load, it becomes evident that lower load ranges, up to 15 bar IMEP, predominantly exhibit initial ignitions in the accumulation area near IV1, as demonstrated in Figure 12. As the load increases, the initial ignitions occur more frequently in the lower-left region of the FOV on the intake side. They are generally more widely distributed throughout the combustion chamber. This shift can be attributed to increased turbulence and enhanced mixing within the combustion chamber.

Increased load at constant engine speed and constant AFR leads to a rise in the inlet mass flow. Given the constant volume flow and inlet temperature, this mass flow increase causes a corresponding density increase. Consequently, the higher density amplifies the inertial forces, manifesting as increased turbulence. This elevated turbulence might alter the mixture distribution within the combustion chamber, causing the previously localized rich area to shift or dissipate entirely.

The temperature increase resulting from the load enhancement leads to an elevated heat input into the engine components. In addition to the pre-

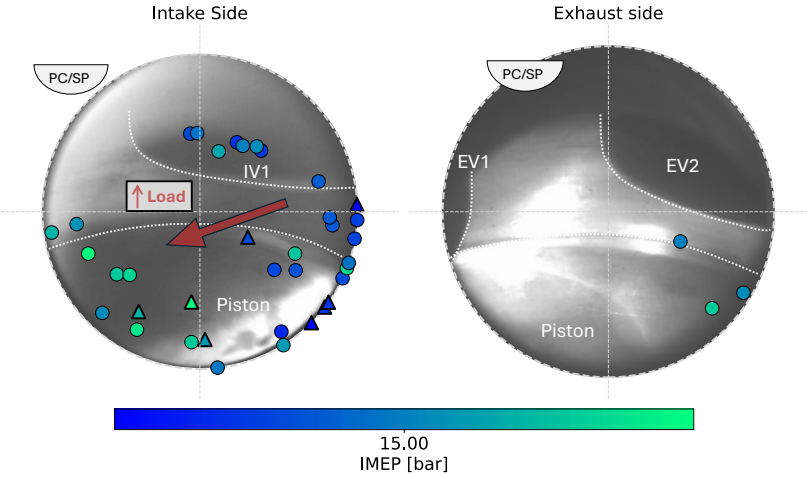

Figure 12: Load dependent initial Ignition position distribution of backfire events with pre-chamber (circle) and open chamber (triangle) ignition system. λ = 2.3 – 4.0.

chamber tip and EVs, the piston's flame deck is also affected. A rise in surface temperature could potentially be an additional cause of piston-side ignition.

Thus, the increase in load contributes to the observed changes in ignition distribution due to the modified mixture stratification. The initial ignitions become more dispersed throughout the combustion chamber and appear to originate increasingly from the direction of the heated piston during its negative stroke movement.

The behavior of the initial ignition position, as well as the load distribution, is independent of the investigated ignition system.

6 CONCLUSIONS

The present study investigated combustion anomalies in a medium-speed, single-cylinder research engine with a displacement volume of 42.3 L. Two endoscopic accesses were used to capture high-speed recordings of emissions in the visible range and emissions of the OH radical. The influence of AFR variations between 2.3 and 4.0 and the ignition concepts of an active pre-chamber and an open combustion chamber were analyzed. After post-processing, regular combustion events were visualized, showing the flame propagation following ignition and highlighting the omnipresence of oil in the combustion chamber. Thermal blackbody radiation and glowing oil droplets observed during pre-chamber operation when used with synthetic oil emphasize the constant risk of LOI.

The combustion anomalies recorded under the specified parameter variations can be categorized into backfire and pre-ignition events. The origins of these anomalies and initial detections were distributed throughout the combustion chamber, with an increased occurrence observed in the region around IV1. This localized phenomenon can be attributed to a hydrogen accumulation caused by density separation in the intake manifold. The laterally curved intake configuration results in a longer flow path to IV2, resulting in a leaner mixture on the path to IV2. The corresponding richer mixture on the path to IV1 favors to be the origin of abnormal combustion.

It could be shown that at low to medium loads (IMEP < 15 bar), the combustion origin is in the range of enrichment. For increased loads, however, there is distribution throughout the combustion chamber with increased piston-side occurrence. The increase in load leads to an increase in density at constant speed, which influences the turbulence and, thus, the mixing behavior in the combustion chamber. The local enrichment appears to shift or even dissolve, which distributes the combustion anomaly origins in the combustion chamber.

A temporal or spatial dependency on the AFR could not be identified.

The results indicate a dependence of the mixture distribution in the combustion chamber on the origins of anomalous combustion. The geometry of the intake manifold plays a decisive role for local inhomogeneity. The ignition concept appears to play a secondary role in the origin of the anomaly.

The results obtained must be supplemented with additional parameter variations in engine operation. Realigning the optical access points between valves IV1 and EV1 could provide deeper insights into the combustion origins in the regions where anomalies occur. Furthermore, installing temperature measurement points in the intake manifold and 3D CFD analyses would enable a more comprehensive classification of the results.

To reduce reactivity, enhance charge cooling, and improve mixture homogeneity, the visual investigation of EGR as a performance-enhancing measure should be considered.

7 DEFINITIONS, ACRONYMS, ABBREVIATIONS

COV	Coefficient of variance
DI	Direct injection
EGR	Exhaust gas recirculation
EV	Exhaust valve
FOV	Field of view
HydroPoLEN	Hydrogen Powered Large Engines
IMEP	Indicated mean effective pressure
IV	Intake valve
LOI	Lube oil ignition
PFI	Port fuel injection
SOI	Start of injection
T	Transmission

TDC	Top dead center
UV	Ultra-violet

8 ACKNOWLEDGMENTS

This work was part of the “Hydrogen Powered Large Engine (HydroPoLEn)” project, FKZ 03SX570B, and was funded by the Federal Ministry of Economics and Climate Protection of the Federal Republic of Germany. This project is in cooperation with MAN Energy Solutions ES, WTZ Roßlau, Tenneco, Carnival Corporation & PLC, and the Institute of Sustainable Mobile Powertrains at the Technical University of Munich. Their support and contribution are gratefully acknowledged.

9 CONTACT

Sven Ole Deist, M.Sc.
Technische Universität München
School of Engineering and Desing
Department of Mobility Systems Engineering
Chair of Sustainable Mobile Powertrains
Schragenhofstraße 31, 80992 Munich, Germany
s-o.deist@tum.de

10 REFERENCES

[1] Ampah, J. D.; Jin, C.; Afrane, S.; Yusuf, A. A.; Liu, H. and Yao, M. 2024. Race towards net zero emissions (NZE) by 2050: reviewing a decade of research on hydrogen-fuelled internal combustion engines (ICE), *Green Chemistry*, 26: 9025–9047.

[2] Stępień, Z. 2021. A Comprehensive Overview of Hydrogen-Fueled Internal Combustion Engines: Achievements and Future Challenges, *Energies*, 14: 6504.

[3] NOW GmbH. 2021. *Wasserstoffverbrennungsmotor als alternativer Antrieb*, Berlin, Germany.

[4] Kolahchian Tabrizi, M.; Cerri, T.; Bonalumi, D.; Lucchini, T. and Brenna, M. 2024. Retrofit of Diesel Engines with H2 for Potential Decarbonization of Non-Electrified Railways: Assessment with Lifecycle Analysis and Advanced Numerical Modeling, *Energies*, 17: 996.

[5] Verhelst, S. and Wallner, T. 2009. Hydrogen-fueled internal combustion engines, *Progress in Energy and Combustion Science*, 35: 490–527.

[6] DECHEMA, acatech (Ed.). 2024. *Comparative analysis of international hydrogen strategies, Country analysis 2023*, Frankfurt, Germany.

[7] International Energy Agency. 2024. *World Energy Outlook 2024*, Paris, France.

[8] Deutsches Zentrum für Luft- und Raumfahrt e. V. (DLR) Institut für Maritime Energiesysteme. 2022. *Zukünftige maritime Treibstoffe und deren mögliche Importkonzepte*, Geesthacht, Germany.

[9] ISO. *ISO/TR 15916:2015(E)*. *Basic considerations for the safety of hydrogen systems*. 2015. ISO, Geneva, Switzerland.

[10] Gao, J.; Wang, X.; Song, P.; Tian, G. and Ma, C. 2022. Review of the backfire occurrences and control strategies for port hydrogen injection internal combustion engines, *Fuel*, 307: 121553.

[11] Klell, M.; Eichlseder, H. and Trattner, A. 2018. *Wasserstoff in der Fahrzeugtechnik*, 4th ed. Springer Fachmedien Wiesbaden, Wiesbaden, Germany.

[12] Guiberti, T. F.; Belhi, M.; Damazo, J. S.; Kwon, E.; Roberts, W. L. and Lacoste, D. A. 2020. Quenching distance of laminar methane-air flames at cryogenic temperatures and implications for flame arrester design, *Applications in Energy and Combustion Science*, 1-4: 100001.

[13] Eicheldinger, S.; Waligorski, D.; Wachtmeister, G. and Jaensch, M. 2022. Performance Potential of Hydrogen Combustion Engines for Industrial Applications, *MTZ worldwide*, 83: 60–64.

[14] Grabner, P.; Schneider, M. and Gschiel, K. 2023. Formation Mechanisms and Characterization of abnormal Combustion Phenomena of Hydrogen Engines. *2023 JSAE/SAE Powertrains, Energy and Lubricants International Meeting*, Kyoto, Japan.

[15] Gleis, S. M. 2023. *Optische Untersuchung eines diffusiven Dual-Fuel Brennverfahrens für Erdgas sowie alternative*. TU Munich, Munich, Germany.

[16] Karmann, S. B.; Röhrle, H.; Klier, B.; Prager, M. and Wachtmeister, G. 2022. Design of an Endoscopic Fully Optically Accessible High-Speed Large-Bore Engine, *SAE International Journal of Engines*, 15.

[17] Li, Y.; Liu, B.; Qin, S.; Chang, W. and Dong, Q. 2023. Experimental study on flame combustion characteristics of large-bore marine diesel engine based on endoscopic technology, *Case Studies in Thermal Engineering*, 44: 102856.

[18] Karmann, S.; Eicheldinger, S.; Prager, M.; Jaensch, M. and Wachtmeister, G. 2023. Experimental comparison between an optical and an all-metal large bore engine, *International Journal of Engine Research*, 24: 1223–1238.

[19] Eicheldinger, S.; Karmann, S.; Prager, M. and Wachtmeister, G. 2022. Optical screening investigations of backfire in a large bore medium speed hydrogen engine, *International Journal of Engine Research*, 23: 893–906.

[20] Distaso, E.; Calò, G.; Amirante, R.; Palma, P. de; Mehl, M.; Pelucchi, M.; Stagni, A. and Tamburrano, P. 2022. Highlighting the Role of Lubricant Oil in the Development of Hydrogen Internal Combustion Engines by means of a Kinetic Reaction Model, *Journal of Physics: Conference Series*, 2385: 12078.

[21] Distaso, E.; Calò, G.; Amirante, R.; Baloch, D. A.; Palma, P. de and Tamburrano, P. 2023. Can lubricant oil promote undesired self-ignition of the charge in hydrogen engines?, *Journal of Physics: Conference Series*, 2648: 12084.

[22] Distaso, E.; Calò, G.; Amirante, R.; Palma, P. de; Mehl, M.; Pelucchi, M.; Stagni, A. and Tamburrano, P. 2025. Linking lubricant oil contamination to pre-ignition events in hydrogen engines–The HyLube mechanism, *Fuel*, 379: 133041.

[23] Gschiel, K.; Wilfling, K. and Schneider, M. 2024. Development of a method to investigate the influence of engine oil and its additives on combustion anomalies in hydrogen engines, *Automotive and Engine Technology*, 9: 1–15.

[24] Lauer, M. 2011. *Determination of the Heat Release Distribution in Turbulent Flames by Chemiluminescence Imaging*, Munich, Germany.

[25] Vera-Tudela, W.; Süess, P.; Albrecht, P.; Wüthrich, S. and Herrmann, K. 2024. Experimental study of lube oil pre-ignition in an optical gas engine test rig, *International Journal of Engine Research*, 25: 1037–1049.

[26] Feng, D.; Buresheid, K.; Zhao, H.; Wei, H. and Chen, C. 2019. Investigation of lubricant induced pre-ignition and knocking combustion in an optical spark ignition engine, *Proceedings of the Combustion Institute*, 37: 4901–4910.

[27] Yang, Z.; Wu, J.; Yun, H.; Zhang, H. and Xu, J. 2022. Diagnosis and control of abnormal combustion of hydrogen internal combustion engine based on the hydrogen injection parameters, *International Journal of Hydrogen Energy*, 47: 15887–15895.

[28] Diéguez, P. M.; Urroz, J. C.; Sáinz, D.; Machin, J.; Arana, M. and Gandía, L. M. 2018. Characterization of combustion anomalies in a hydrogen-fueled 1.4 L commercial spark-ignition engine by means of in-cylinder pressure, block-engine vibration, and acoustic measurements, *Energy Conversion and Management*, 172: 67–80.

[29] Laichter, J.; Kaiser, S. A.; Rajasegar, R. and Srna, A. 2024. Optical Investigation of Mixture Formation in a Hydrogen-Fueled Heavy-Duty Engine with Direct-Injection, *SAE Int. J. Adv. & Curr. Prac. in Mobility*, 6(2): 593–612.

[30] Scalambro, A.; Piano, A.; Millo, F.; Scinicariello, N.; Lodi, W.; Dhongde, A. and Sammito, G. 2024. Numerical analysis of the hydrogen-air mixture formation process in a direct-injection engine for off-road applications, *International Journal of Hydrogen Energy*, 77: 1286–1295.

[31] Rajasegar, R. and Srna, A. 2024. On the Phenomenology of Hot-Spot Induced Pre-Ignition in a Direct-Injection Hydrogen-Fueled, Heavy-Duty, Optical-Engine, *SAE Int. J. Adv. & Curr. Prac. in Mobility*, 6(3): 1535–1547.

[32] Wittek, K.; Cogo, V. and Prante, G. 2024. Full load optimization of a hydrogen fuelled industrial engine, *International Journal of Hydrogen Energy*, 77: 230–243.

[33] Novella, R.; García, A.; Gomez-Soriano, J. and Fogué-Robles, Á. 2023. Exploring dilution potential for full load operation of medium duty hydrogen engine for the transport sector, *Applied Energy*, 349: 121635.

[34] Lu, Y.; Que, J.; Liu, M.; Zhao, H. and Feng, L. 2024. Study on backfire characteristics of port fuel injection single-cylinder hydrogen internal combustion engine, *Applied Energy*, 364: 123110.

[35] Shinde, B. J. and K., K. 2022. Recent progress in hydrogen fuelled internal combustion engine (H2ICE) – A comprehensive outlook, *Materials Today: Proceedings*, 51: 1568–1579.

[36] Mitsui E&S Co. 07.03.2024. *World's First Successful Hydrogen Combustion Operation with a Large Marine Engine*. https://www.mes.co.jp/english/press/2024/0307_002400.html, Tokio, Japan. [Accessed 14.01.2025].